

# Surface acoustic waves for acousto-optic modulation in buried silicon nitride waveguides.

Marco A. G. Porcel<sup>1</sup>, Remco Stoffer<sup>2</sup>, Matthijn Dekkers<sup>3</sup>, Marcel Hoekman<sup>4</sup>, Ronald Dekker<sup>4</sup>, Arne Leinse<sup>4</sup>, Peter J. M. van der Slot<sup>\*1</sup>, and Klaus-J. Boller<sup>1</sup>

<sup>1</sup>Laser Physics and Nonlinear Optics, MESA+ Institute for Nanotechnology, University Twente, The Netherlands

<sup>2</sup>PhoeniX Software B.V., Capitoool 50, 7521 PL Enschede, The Netherlands

<sup>3</sup>Solmates B.V., Drienerlolaan 5, building 46, 7522 NB Enschede, The Netherlands

<sup>4</sup>LioniX International B.V., Hengelosestraat 500, 7521 AN Enschede, The Netherlands

September 20, 2022

## Abstract

We theoretically investigate the use of Rayleigh surface acoustic waves (SAWs) for refractive index modulation in optical waveguides consisting of amorphous dielectrics. Considering low-loss  $\text{Si}_3\text{N}_4$  waveguides with a standard core cross section of  $4.4 \times 0.03 \mu\text{m}^2$  size, buried  $8\text{-}\mu\text{m}$  deep in a  $\text{SiO}_2$  cladding we compare surface acoustic wave generation in various different geometries via a piezo-active, lead zirconate titanate film placed on top of the surface and driven via an interdigitized transducer (IDT). Using numerical solutions of the acoustic and optical wave equations, we determine the strain distribution of SAW modes under resonant excitation, and the electric field distribution of the fundamental optical mode near the waveguide core. From the overlap of the acoustic strain field with the optical mode field we calculate and maximize the attainable amplitude of index modulation in the waveguide. For the example of a near-infrared wavelength of  $840 \text{ nm}$ , a maximum relative refractive index modulation of  $1.2 \times 10^{-3}$  was obtained for an IDT period of  $30 \mu\text{m}$ , a film thickness of  $4 \mu\text{m}$ , and using an IDT voltage and modulation frequency of  $10 \text{ V}$  and  $90 \text{ MHz}$ , respectively. This relative index change is about 300-times higher than in previous work based on non-resonant proximity piezo-actuation, and the modulation frequency is about 200-times higher. Exploiting the maximum relative index change of  $1.2 \times 10^{-3}$  in a Mach-Zehnder modulator should allow full-contrast modulation in devices as short as  $120 \mu\text{m}$ .

---

\*Corresponding author: [p.j.m.vanderslot@utwente.nl](mailto:p.j.m.vanderslot@utwente.nl)

# 1 Introduction

Integrated optical waveguides fabricated from stoichiometric silicon nitride ( $\text{Si}_3\text{N}_4$ ) using low pressure chemical vapour deposition (LPCVD) can offer ultra-low loss, are transparent from visible to near-infrared wavelengths [1, 2] and, therefore, are of high interest for numerous applications. These include communications [3], sources for nonlinear microscopy [4], optical coherence tomography [5], biosensors [6], microwave photonics [7, 8], ultra-narrow bandwidth hybrid lasers [9] and supercontinuum generation [4, 10]. Due to a high index contrast with regard to the  $\text{SiO}_2$  cladding, these waveguides enable dense, complex and reconfigurable integrated photonic circuits [11–13].

Typically, light modulation in silicon nitride waveguides relies on the thermo-optic effect and is based on a thermally induced phase shift between the two arms of a Mach-Zehnder interferometer [14]. State-of-the-art thermo-optic modulators provide up to 1 kHz modulation speed, while the dissipation of heating power is often undesired, because it can be as large as 500 mW per modulator [7]. Applications that rely on a high density of modulators, *e.g.*, as in reconfigurable photonic circuits [12], would greatly benefit from modulation techniques with lower dissipation, while applications needing fast modulation of the light would greatly benefit from techniques with higher switching or modulation speeds. A technique, which may provide both benefits simultaneously, may be based on the strain-optic effect [15, 16] where stress induced in the waveguide results in a change of the effective refractive index. The strain-optic effect has been studied in various integrated photonic systems [17, 18]. Specifically in the waveguide platform investigated here (LPCVD  $\text{Si}_3\text{N}_4/\text{SiO}_2$ ) there is so far only a single implementation. In [18], Hosseini *et al.* showed an approach with a 2  $\mu\text{m}$ -thick layer of crystalline lead zirconate titanate (PZT) deposited on top of a silicon nitride Mach-Zehnder interferometer (MZI) with the core of the waveguides positioned 8  $\mu\text{m}$  below the PZT layer. Via an electrode placed on top of the PZT layer above one of the interferometer arms of the MZI, the stress within that arm could be locally controlled via the electrode voltage. The power consumption was reduced significantly, by six order of magnitude. Also the modulation frequency could be raised, up to 600 kHz (at -3 db bandwidth). However, further increasing the modulation frequency was not possible. In that approach this would require a smaller capacitance resulting in a reduced electrode area, but this would reduce the induced stress and thereby the induced index change. The maximum index modulation remained rather small, at around  $5 \times 10^{-6}$  with an optimum geometry. This reduces the overall induced phase shift as required for decreasing the arm length of the interferometer.

Much higher modulation frequencies are possible with a more sophisticated electrode structure, using so-called interdigital transducers (IDTs) that resonantly excite surface acoustic waves (SAWs). For instance, optical modulation at a frequency of 520 MHz was demonstrated for a compact MZI consisting of conventional ridge waveguides of GaAs with an active region of only 15  $\mu\text{m}$  [19], while acousto-optic modulation of photonic resonators on thin polycrystalline aluminum nitride films has been demonstrated for modulation frequencies reaching well into the microwave range [20, 21]. In  $\text{Si}_3\text{N}_4$  stress-induced optical modulation at frequencies above the MHz are not yet available.

Here, we theoretically investigate exploiting SAW-induced effective refractive index changes for realizing faster and smaller modulators with  $\text{Si}_3\text{N}_4$  waveguides.

Using numerical methods we calculate the index modulation experienced by the fundamental optical mode propagating through a  $\text{Si}_3\text{N}_4$  core buried in a  $\text{SiO}_2$  cladding. The special interest in this particular geometry is that no deterioration of the ultra-low optical propagation loss is expected. The reason for that is that the cladding is assumed to be thick enough to make the optical field negligible at the location of the thin PZT film that is on top of the cladding. At the same time, the penetration depth of SAWs is large enough, on the order of the acoustic wavelength,  $\lambda_R$ , in the material [22, 23], which allows for a good overlap of the SAW with the optical wave even for high modulation frequencies in the 100 MHz range. The SAW is considered to be launched using an IDT. Compared to the unstructured electrode arrangement used by Hosseini *et al.* [18], we show below that the fine structuring of the IDT allows typically 200-times higher modulation frequencies while resonant excitation yields a 300-fold increase in index modulation. Another advantage of employing SAWs is that tensile strain can be applied in one interferometer arm, simultaneously applying compressive strain in the other arm, which effectively reduces the length of the arms by a factor of two to obtain full light modulation [19].

In the following we consider acousto-optic modulation using a MZI, in a setting where the acoustic wave propagates perpendicular to the optical waveguide axis of the two arms of the MZI as shown in Fig. 1. We briefly discuss the relation between strain and the refractive index and the surface acoustic wave of interest. We then present the geometry studied and how the simulations are performed. We investigate how the induced strain and, consequently, the effective refractive index, depends on the thickness of the PZT layer and the period of the IDT used to generate the SAW. Finally, we use the maximum change in effective refractive index to determine the required length of the MZI to obtain full modulation of the optical wave. The maximum relative change of the effective waveguide index in our arrangement was found to be 0.12 %, at a frequency of 90 MHz, which yields full modulation with a relatively short arm length of 120  $\mu\text{m}$ , *i.e.*, about 80-times shorter than the proximity piezo methods described above.

## 2 Acousto-optic refractive index modulation

The response of a material to an applied electric field, an acoustic wave, or a combination of the two, strongly depends on the type of material. Here, we are interested on one hand in generating a strong acoustic wave using the piezoelectric effect [24, 25]. On the other hand, we intend to use strain in amorphous waveguide core ( $\text{Si}_3\text{N}_4$ ) and cladding ( $\text{SiO}_2$ ) materials (which do not possess a piezoelectric effect) to cause strain-induced changes in refractive index [24, 25]. The strain can be compressive or tensile, leading to an increase or decrease in local refractive index, respectively. In a microscopic picture, strain changes both the number of microscopic dipoles per unit volume and the microscopic potential. This volume change determines the induced dipole driven by the applied optical field and thus changes the optical susceptibility tensor,  $\chi$ , of the material. In the most general case of an anisotropic material, the relation between the change in the inverse of the dielectric tensor and the applied strain is given by [16, 26],

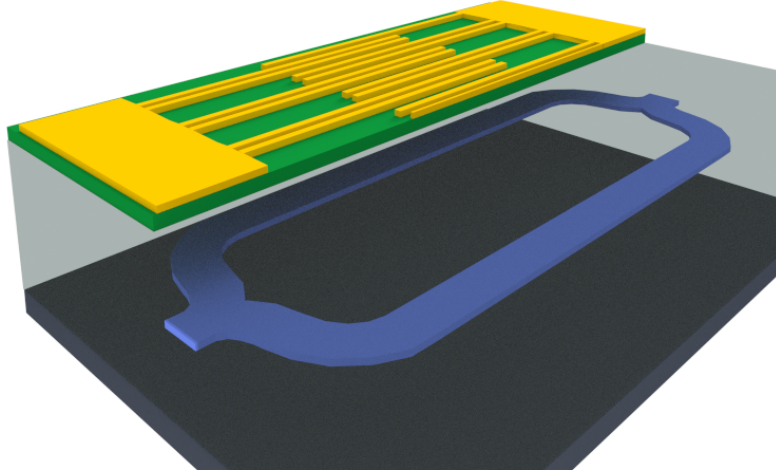


Figure 1: Artistic impression of a waveguide (in blue) based Mach-Zehnder interferometer. Half of the electrode structure and piezo layer is not shown to enable a full view on the interferometer (dark blue waveguides). The interferometer waveguides are buried in SiO<sub>2</sub> (light grey) deposited on a silicon substrate (dark grey).

$$[\Delta(\varepsilon^{-1})]_{ij} = (\mathbf{pS})_{ij} = \sum_{kl} \mathbf{p}_{ijkl} \mathbf{S}_{kl}, \quad (1)$$

where  $\varepsilon = \varepsilon_0(\mathbf{1} + \boldsymbol{\chi})$  is the dielectric tensor,  $\varepsilon_0$  is the vacuum permittivity,  $\mathbf{S}$  is the strain tensor and  $\mathbf{p}$  is the dimensionless strain-optic tensor. The indices,  $i, j, k$  and  $l$  designate the three Cartesian coordinates. For isotropic materials such as the amorphous materials investigated here, and assuming small changes in the inverse dielectric tensor, eq. 1 can be simplified. In this case, the related change in refractive index is given by [27, 28]

$$\Delta n_x = -\frac{1}{2} n_0^3 (p_{11} S_x + p_{12} S_y). \quad (2)$$

Here,  $\Delta n_x$  is the change in refractive index for linear polarized light along the  $x$  direction,  $n_0$  is the refractive index of the material in absence of any strain,  $S_i$  is the strain applied in the  $i$ -direction ( $i = x, y$ ) and the contracted indices notation is used [16]. The change in refractive index for the other polarization direction is obtained via exchanging the strain-tensor components,

$$\Delta n_y = -\frac{1}{2} n_0^3 (p_{12} S_x + p_{11} S_y). \quad (3)$$

In this work, strain in the region of the optical mode is induced by an acoustic wave. As the optical mode is confined to an area just a few micrometer below the surface of the cladding, for obtaining a strong interaction, the surface acoustic wave (SAW) is the most appropriate acoustic wave to consider for a strong interaction. The reason is that a SAW travels along the surface of an elastic material with most of its energy and strain confined within a small region,

with a thickness of the order of the acoustic wavelength, below the surface and thus can provide good overlap between the strain induced by the SAW and the optical mode. Of various different surface waves possible, we focus on Rayleigh surface acoustic waves, which are characterized by a correlated transverse and longitudinal motion at the surface. This results in volume elements traversing an elliptical path when the wave passes [29]. The motivation to investigate Rayleigh waves is that the considered SAW<sup>1</sup> has low dispersion, as long as the elastic modulus near the surface does not change [29], making them suitable for the modulation of broadband signals [30].

If the SAW is launched perpendicular to the two arms of a MZI as depicted in Fig 2, and the two arms of length  $L$  are separated by half an acoustic wavelength, one arm experiences compressive strain and the other tensile strain. The phase shift of light leaving either interferometer arm with respect to the light entering the interferometer is given by

$$\Delta\varphi = 2\pi\Delta n\frac{L}{\lambda}, \quad (4)$$

where  $\Delta n$  is the change in effective refractive index,  $n_{\text{eff}}$ , of the optical mode, which is opposite in sign for the two arms,  $n_{\text{eff}} = \frac{c\beta}{\omega}$ ,  $c$  is the speed of light in vacuum,  $\beta$  is the propagation constant for the fundamental mode,  $\omega$  is the light frequency and  $\lambda$  is the vacuum wavelength. When the light is combined at the output of the MZI, the total phase difference is

$$\Delta\varphi_t = 4\pi|\Delta n|\frac{L}{\lambda}. \quad (5)$$

A total phase difference of  $\Delta\varphi_t = \pi$  is required for full light modulation. Therefore, when the length  $L$  is equal to

$$L = \frac{\lambda}{4|\Delta n|}, \quad (6)$$

light is fully modulated with a modulation frequency equal to the frequency of the SAW. The latter equation shows that a weak index modulation (small  $\Delta n$ ) would require long arm lengths or interaction lengths, which is undesired for compact, integrated waveguide circuits with a high density of components.

For providing full modulation also with short interaction lengths, a SAW is ideally created in a material having a large piezoelectric coefficient. For our calculations we consider lead zirconate titanate (PZT), because PZT is known as high performance piezoelectric material and commonly used in actuators and sensors [31]. Another advantage is that thin PZT layers have already been successfully deposited on  $\text{Si}_3\text{N}_4$  waveguides in a  $\text{SiO}_2$  cladding [18] by using a Ti/Pt bilayer as seed for epitaxial growth of the PZT [18] on top of the amorphous  $\text{SiO}_2$  cladding material. The PZT layer may be grown using pulsed laser deposition [18] or alternative techniques like liquid-phase growth [32]. The different seeding techniques allow configurations with and without a conducting layer between the amorphous cladding and crystalline PZT. The generation and comparison of SAWs in various such geometries is presented in the next section.

---

<sup>1</sup>SAW refers to a Rayleigh surface acoustic wave in the remainder of this work.

### 3 Geometry and simulation domain

The geometries considered here are shown schematically in Fig. 2(a) and as cross-sections in (b-f). The optical design comprises a typical low-loss optical waveguide having a  $\text{Si}_3\text{N}_4$  core of height 30 nm and width  $4.4 \mu\text{m}$  embedded symmetrically in a  $16 \mu\text{m}$  thick  $\text{SiO}_2$  cladding on top of a Si wafer substrate, *i.e.*, at  $8 \mu\text{m}$  distance from the Si and  $\text{SiO}_2$  interfaces. The strain-optic tensor is not known for  $\text{Si}_3\text{N}_4$ . However, due to the small core thickness the optical mode is mostly outside the core and a modulation of the effective refractive index is dominantly caused by the strain-optic effect in the  $\text{SiO}_2$  cladding. The thickness of the cladding,  $8 \mu\text{m}$ , is taken big enough that the optical mode does not extend to the end of the cladding, in order to render optical losses due to surface layers or the substrate negligible. The top of the  $\text{SiO}_2$  cladding contains a thin conductive or dielectric seeding layer that allows the growth of c-oriented PZT. The thickness,  $d$ , of the PZT layer was varied to determine the optimum thickness for excitation of the SAW. A split-finger IDT configuration is used to excite the SAW without first order Bragg reflections [30]. In order to maximize the optical modulation amplitude, we investigate the effect of the location of the conductive (*i.e.* gold) electrodes of the IDT and a seeding layer in four different configurations.

The first consists of the IDT electrodes at the PZT-air interface and a conductive seeding layer at the  $\text{SiO}_2$ -PZT interface (**ETC**, Fig. 2(c)). The second, consists of the IDT electrode on top of the PZT layer with a dielectric seed layer (shown in blue) (**ETD**, Fig. 2(d)). The third and fourth configurations have the IDT electrode at the  $\text{SiO}_2$ -PZT interface and have a conductive layer (**EBC**, Fig. 2(e)) or simply a bare PZT-air interface (**EBD**, Fig. 2(f)). Configurations **EBC** and **EBD** have both a thin seed dielectric nanosheet deposited on top of the IDT electrode to allow crystalline growth of the PZT layer. Because the seed dielectric layer is only a few nm thick and is considered to have perfect adhesion to  $\text{SiO}_2$  it would not notably affect the acoustic wave, and is not included in the model.

The IDT generates a SAW and the associated strain induces a change in refractive index in both the cladding and the core. However, the optical modulation amplitude is expected to depend on the strain distribution of the excited SAW and its overlap with the optical mode. In order to determine the degree of overlap, the strain distribution is calculated by finding the fundamental SAW eigenmode for the four configurations using a finite-element eigenmode solver [33]. For these calculations, we use the two-dimensional unit cell shown in Fig. 2(b), which consists of one period of the split finger IDT electrode and the layers below (and layers above in case of configurations **EBC** and **EBD**). To maximize the strain at the location of the optical mode, the waveguide core is positioned in the horizontal direction,  $x$ , in Fig. 2, to lie symmetrically underneath the gap of two IDT electrodes. Platinum is selected for the conductive seed layer material (gray) and gold (yellow) for the conductive layer on top of the PZT. Both layers as well as the gold electrodes of the IDT are taken as 100 nm thick.

The acoustic boundary conditions applied to the unit cell are a free displacement condition at the air interface, a zero displacement condition at the bottom of Si substrate and a periodic boundary condition at the two remaining boundaries. In order to ensure that the SAW has negligible amplitude near the

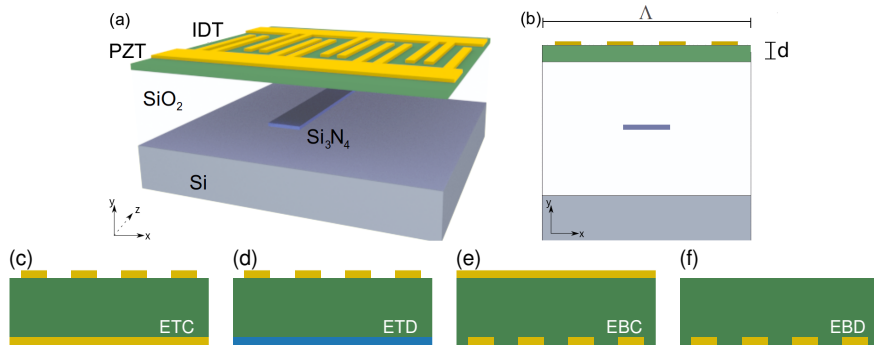


Figure 2: (a) Schematic view of the geometry comprising a  $\text{Si}_3\text{N}_4$  core ( $4.4 \times 0.03 \mu\text{m}$ , dark blue) centered in a  $16\text{-}\mu\text{m}$  thick  $\text{SiO}_2$  cladding (light gray) on a Si substrate (dark gray). A crystalline PZT layer on top of the cladding (green) in combination with an IDT (yellow) is used for exciting surface acoustic waves (SAWs). (b) The cross-section shows the corresponding two-dimensional unit cell across a single period  $\Lambda$  of the IDT and the layers below it. The thickness of the Si layer included in the unit cell is proportional to  $\Lambda$  to ensure a negligible SAW amplitude at the lower boundary of the unit cell. The layer between the PZT and the  $\text{SiO}_2$  layers is either conductive (yellow) or dielectric (light blue) and functions as seed layer for the crystalline growth of the PZT layer on top of the amorphous  $\text{SiO}_2$  or IDT electrode. (c)-(f) Illustrate the various combinations of IDT locations with and without opposite conductive layer, following the same color coding. (c) ETC, (d) ETD, (e) EBC, (f) EBD. Features are not to scale.

bottom of the substrate and the zero displacement boundary condition does not affect the solution, the height of the Si substrate was found not to affect the solutions for heights larger than  $5\Lambda$ , where  $\Lambda$  is the period of the IDT electrode.

For the calculation of the optical field distribution, the optical boundary conditions were taken as zero-field conditions at all outer boundaries. This is well-justified because with the chosen index and size parameters the optical field is confined closely around the core as compared to the thickness of the cladding. The refractive indices for the  $\text{Si}_3\text{N}_4$  core and  $\text{SiO}_2$  cladding materials are taken from Luke *et al.* [34].

To calculate the resonant acoustic frequencies for each of the configurations as a function of both the thickness,  $d$ , of the PZT layer and period,  $\Lambda$ , of the IDT electrode, we used an eigenmode solver. Note that a resonant frequency corresponds to the modulation frequency of the light in a properly configured Mach-Zehnder interferometer. To determine the effective refractive index at the location of the optical mode, it is required that the applied voltage is chosen to oscillate at the resonant frequency. The electro-mechanical coupling coefficient was obtained by performing a frequency-domain simulation using the same unit cell as shown in Fig. 2(b) and calculating the strain distribution when a sinusoidal voltage with a given amplitude (we chose 10 V) and a frequency equal to the resonant acoustic frequency is applied to the IDT electrode. Also for this study, we investigated the dependence of the induced strain on  $d$  and  $\Lambda$ . The various isotropic material properties used in the simulation are listed in table

Table 1: Material constants used in calculating the SAW properties. Parameters not included in the model are denoted as (NI). Parameters included in tensor form are shown as (-).

Material constants				
	Young's Modulus GPa	Poisson's Ration	Density kg/m <sup>3</sup>	Damping factor, $\eta$
Pt	168	0.38	21450	NI
Au	54	0.44	19300	NI
PZT	-	-	7600	0.03
SiO <sub>2</sub>	70	0.17	2650	0.0004
Si <sub>3</sub> N <sub>4</sub>	270	0.24	3440	NI
Si	-	-	2330	NI

1 [33, 35–37]. The elasticity matrix  $C$  used for PZT and silicon in the simulation is given by [36]

$$C = \begin{pmatrix} c_{11} & c_{12} & c_{21} & 0 & 0 & 0 \\ c_{12} & c_{11} & c_{21} & 0 & 0 & 0 \\ c_{21} & c_{21} & c_{33} & 0 & 0 & 0 \\ 0 & 0 & 0 & c_{44} & 0 & 0 \\ 0 & 0 & 0 & 0 & c_{44} & 0 \\ 0 & 0 & 0 & 0 & 0 & c_{66} \end{pmatrix}, \quad (7)$$

where the coefficients for PZT are  $c_{11} = 134.8$  GPa,  $c_{12} = 63.9$  GPa,  $c_{21} = 68.1$  GPa,  $c_{33} = 113.3$  GPa,  $c_{44} = 22.2$  GPa and  $c_{66} = 33.4$  GPa. For silicon there are only three independent coefficients  $c_{11} = c_{33} = 165.7$  GPa,  $c_{12} = c_{21} = 63.9$  GPa, and  $c_{44} = c_{66} = 51.0$  GPa. The piezoelectric coupling tensor,  $\mathbf{d}$ , is given by [37]

$$\mathbf{d} = \begin{pmatrix} 0 & 0 & 0 & 0 & 440 & 0 \\ 0 & 0 & 0 & 440 & 0 & 0 \\ -60 & -60 & 152 & 0 & 0 & 0 \end{pmatrix} \times 10^{-12} \frac{\text{C}}{\text{N}}, \quad (8)$$

and the relative permittivity tensor,  $\epsilon^T$ , is given by [37]

$$\epsilon^T = \begin{pmatrix} 990 & 0 & 0 \\ 0 & 990 & 0 \\ 0 & 0 & 450 \end{pmatrix}, \quad (9)$$

where the superscript  $T$  indicates that the relative permittivity tensor is measured under constant stress.

## 4 Results

### 4.1 Acoustic wave generation

We are interested in MZI-based modulation with a maximum optical phase change in the interferometer arms. Therefore we consider a geometry where the SAW propagation direction is perpendicular to the optical axis of the waveguide,

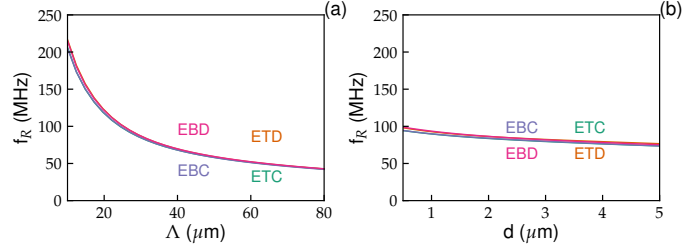


Figure 3: Resonant acoustic frequency,  $f_R$ , of the fundamental Rayleigh wave for the four investigated IDT configurations (ETD, EBD, ETC, EBC, found in Fig. 2). The frequency is displayed as function of the period of the acoustic wave  $\lambda_R$ , which is equal to the period  $\Lambda$  of the IDT for a fixed PZT thickness  $d = 2 \mu\text{m}$  (a), and as a function of the thickness  $d$  of the PZT layer for an IDT period of  $\Lambda = 30 \mu\text{m}$  (b).

as in Figs. 1 and 2. The modulation frequency is taken as equal to the resonant frequency of the fundamental SAW. In this case, the acoustic wavelength,  $\lambda_R$ , and frequency,  $f_R$ , are equal to the period,  $\Lambda$ , and driving frequency of the IDT, respectively. The relation between  $f_R$  and  $\Lambda_R$  is given by

$$f_R = v_R/\Lambda_R, \quad (10)$$

where  $v_R$  is the phase velocity of the SAW. In general,  $v_R$  varies with  $\Lambda$ ,  $d$  and the different IDT configurations such that the modulation frequency of the optical wave will also vary with these parameters.

Figure 3(a) shows the acoustic frequency,  $f_R$ , of the fundamental SAW as a function of the IDT period,  $\Lambda$ , for a fixed PZT layer thickness of  $d = 2.5 \mu\text{m}$  in the four geometries shown in Fig. 2(c-f). Similarly, Fig. 3(b) shows  $f_R$  as a function of the PZT thickness,  $d$ , for a fixed IDT period of  $\Lambda = 30 \mu\text{m}$  and the four geometries.

Figure 3(a) shows that the acoustic frequency monotonically decreases for all configurations as the IDT period increases. It can be seen that for large periods, all four configurations have approximately the same resonant acoustic frequency, while for shorter periods the configurations ETD and EBD possess a slightly higher resonant acoustic frequency compared to the configurations ETC and EBC.

Figure 3(b) shows as well that the frequency decreases monotonically for all configurations as the layer thickness increases. The configurations ETC and EBC show nearly identical resonant acoustic frequencies when the layer thickness is varied. For small layer thickness, the resonant acoustic frequency for configuration EBD is somewhat higher than that produced by configuration ETD. For larger layer thickness, the situation is reversed, *i.e.*, the resonant acoustic frequency for configuration EBD is somewhat lower than that for configuration ETD.

The different resonant acoustic frequencies, found when the thickness of the layer is varied at constant IDT period, indicate that the sound velocity of the acoustic wave is affected by the amount of PZT material present. On the other hand, for a fixed geometry and varying only the IDT period, *i.e.*, the period of the acoustic wave, we observe a strong increase in the resonant frequency when the period decreases (Fig. 3(a)), which is to be expected from the reciprocal

relation between frequency and wavelength (*c.f.* eq. 10). In summary, when the PZT layer is terminated with a conductive layer opposite to the IDT electrode, the resonant acoustic frequency is somewhat lower and is almost independent of the location of the IDT electrode (at PZT-air interface or SiO<sub>2</sub>-PZT interface), while when it is terminated with a dielectric layer, the resonant frequency is somewhat higher and is affected by the location of the IDT electrode.

In order to determine the change in effective refractive index of the fundamental optical mode that is induced by the SAW, the strain distribution generated by the SAW within the volume of the optical mode has to be calculated. A frequency domain analysis is performed to calculate the induced strain when a sinusoidal voltage is applied at a near resonant acoustic frequency to the IDT electrode. We note that with our symmetric unit cell (see Fig. 2(b)) the frequency domain analysis showed zero strain when excited at exactly the resonant frequency. However, when moving the frequency slightly off resonance, a nonzero strain is obtained. Adding acoustic damping to the cladding and piezo regions (see parameters in table 1), provides a physically realistic and numerically stable response.

A typical example of the strain distribution amplitude generated by the fundamental SAW when a voltage signal with an amplitude of 10 V is applied to the IDT electrode is shown in Fig. 4 for the configuration **ETD** with  $\Lambda = 15 \mu\text{m}$  and  $d = 2 \mu\text{m}$ , which corresponds to modulation with  $f_R = 150 \text{ MHz}$ . In this figure, only the region of interest is shown, *i.e.*, the region containing the waveguide's core and cladding. The origin of the coordinate system coincides with the center of the optical waveguide, and  $y = 8 \mu\text{m}$  coincides with the SiO<sub>2</sub>-PZT interface. The  $z$ -axis (along which the optical mode propagates) points along the axis of the waveguide, normal to  $x$  and  $y$ . Figure 4(a) shows the modulus of the induced strain in the  $x$ -direction,  $|S_x|$ , and Fig. 4(b) for strain in the  $y$ -direction,  $|S_y|$ . We observe that with increasing depth,  $|S_x|$  grows from a near-zero value at  $y \approx 8 \mu\text{m}$ , reaching a maximum before decreasing again towards  $y = -8 \mu\text{m}$ . Inspecting  $S_x$  within the PZT layer shows that  $S_x$  changes sign as a function of depth and therefore there is a depth at which  $S_x$  is zero. Note that for the parameters of Fig. 4, this depth is at the upper edge of the region plotted (near the SiO<sub>2</sub>-PZT interface) and moves to smaller  $y$  values, *i.e.*, larger depth below the PZT layer, when  $\Lambda$  increases. In contrast to horizontal strain, the vertical strain,  $S_y$ , does not change sign and  $|S_y|$  decreases monotonically with increasing depth, as seen in Fig. 4(b). Comparison of Figs. 4(a) and (b) shows that  $|S_y|$  is the dominant strain at the location of the waveguide core and is typically a factor of 2 or more larger than  $|S_x|$ . This typical example shows that the SAW-induced strain easily extends to the core of the optical waveguide and, therefore, a good overlap between the induced strain and optical mode is expected.

Two of the other configurations (**EBC** and **EBD**) exhibit similar strain patterns (not separately shown), although with different strength. The remaining configuration, **ETC** displayed a different behaviour in that the induced strain in the cladding region was significantly smaller (about six orders of magnitude) than for the other configurations. Apparently, the presence of the Pt layer between the PZT and SiO<sub>2</sub>, together with the presence of acoustic damping, results in a very poor coupling of the generated SAW into the cladding region. We note that by artificially turning off the acoustic damping, a similar behaviour for the strain was obtained as for the other configurations. In the remainder of this

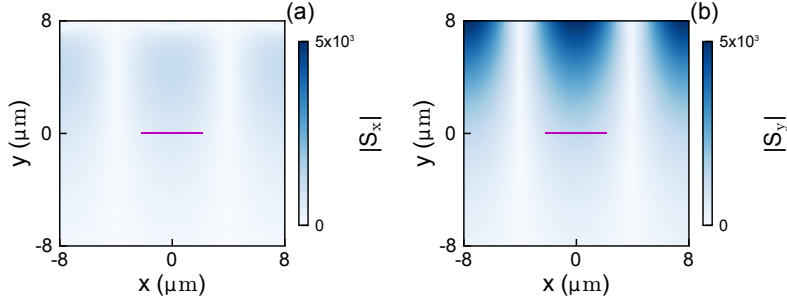


Figure 4: Strain distribution in the horizontal,  $|S_x|$ , and vertical,  $|S_y|$ , directions as generated by the fundamental Rayleigh wave when  $\Lambda = 15 \mu\text{m}$  and  $d = 2 \mu\text{m}$ . The  $\text{Si}_3\text{N}_4$  waveguide core is shown in purple at scale.

work we will only consider the configurations ETD, EBC and EBD.

### Maximizing strain

In order to quantify how the strain can be maximized via variation of the thickness of the PZT layer and the period of the IDT electrode, we plot in Fig. 5(a) the dominant induced strain,  $|S_y|$ , as a function of the IDT period,  $\Lambda$ , for  $d = 2.5 \mu\text{m}$  when a sinusoidal voltage with a near resonant frequency and an amplitude of 10 V is applied to the IDT for the three configurations considered. Similarly, Fig. 5(b) shows  $|S_y|$  as a function of the layer thickness,  $d$ , for  $\Lambda = 25 \mu\text{m}$ .

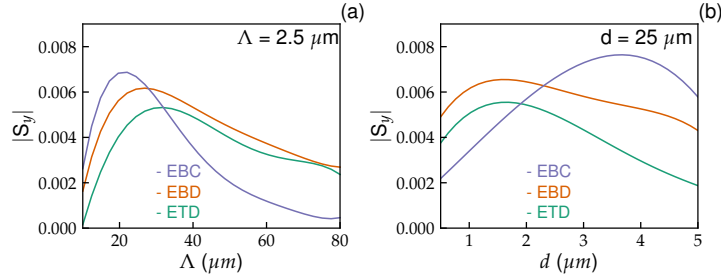


Figure 5: Strain distribution,  $|S_y|$ , in the vertical direction as produced by the fundamental Rayleigh SAW at the center of the optical waveguide as a function of IDT period,  $\Lambda$  for  $d = 2.5 \mu\text{m}$  (a) and as function of the layer thickness,  $d$ , for  $\Lambda = 25 \mu\text{m}$ . Only results for the configurations ETD, EBC and EBD are shown. A sinusoidal voltage with a near resonant frequency and an amplitude of 10 V is applied to the IDT electrode.

It can be seen in Fig. 5(a) that, with increasing IDT period,  $|S_y|$  at the center of the optical waveguide increases before reaching a maximum. Increasing the IDT period further results in a decreasing  $|S_y|$ . The overall dependence of  $|S_y|$  on  $\Lambda$  is very similar for the three configurations, however, it can be seen that EBC produces the largest strain at the center of the waveguide for an IDT period that is smallest for the three configurations. Figure 5(a) also shows an increased

decay of  $|S_y|$  for periods  $\Lambda \gtrsim 25 \mu\text{m}$  for configuration **EBC** compared to the other two configurations. The behaviour of  $|S_y|$  at the center of the optical waveguide can be explained as follows.

As the IDT period increases, the acoustic wavelength of the SAW increases and the wave penetrates deeper into the structure towards the waveguide core. Consequently, the strain,  $|S_y|$ , at the location of the core is expected to increase. However, at the same time the volume corresponding to a single acoustic period increases as well. As the IDT electrode is powered by a constant voltage signal, this results in a decreasing amplitude of the sound wave and, consequently, the induced strain. The balance of these two effects is what gives rise to the maximum observed in Fig. 5(a). The different electric field distribution when a conductive layer is present opposite of the IDT electrode results in a more efficient excitation of the SAW wave for the optimum IDT period and PZT layer thickness combination at the cost of a faster decay in SAW excitation when the combinations moves away from the optimum.

A similar trend is visible in the dependence of  $|S_y|$  on  $d$  as shown in Fig. 5(b) for the three configurations and  $\Lambda = 25 \mu\text{m}$ . Again, the configuration with the 100-nm gold layer on top (**EBC**) provides the largest strain,  $|S_y|$ , at the waveguide core, followed by the configurations **EBD** and **ETD**. We also observe a maximum in the strain as function of the layer thickness,  $d$ , of the PZT layer, although the strain is near maximum over a wide range of thickness values ( $1 \mu\text{m} < d < 3 \mu\text{m}$ ) for configurations **EBD** and **ETD**. Figure 5(b) also shows that for configuration **EBC** the maximum strain is obtained at a larger PZT layer thickness than for the other two configurations. As expected,  $|S_y|$  starts dropping to zero for small values of  $d$ , although much faster for **EBC** than for the other two configurations. As the acoustic wavelength is not changed when the layer thickness is varied, these results show that there is an optimum thickness for the PZT layer to couple the electrical power supplied to the IDT into the SAW wave. This also maximizes the strain at the core of the waveguide, the value of which varies with the IDT period and depends on the configuration used. We attribute the larger maximum strain and higher sensitivity to the PZT layer thickness of configuration **EBC** to the 100-nm thick gold layer on top of the PZT layer, which affects the electric field distribution inside the PZT layer such that it produces the largest-amplitude SAW under optimum conditions.

In summary so far, we find that in order to maximize the acoustic modulation frequency, all configurations require a thin PZT layer and a small IDT period. Of the three configurations studied, **ETD** and **EBD** provide almost equal modulation frequencies for a given  $d$  and  $\Lambda$ , which are somewhat higher than those for the two other configurations. However, the need to create maximum strain in the area of the optical mode requires an optimum IDT period with corresponding optimum PZT layer thickness, which will ultimately limit the maximum modulation frequency (via a decreasing index modulation) that can be realized.

## 4.2 Modulation of the effective refractive index

In this section we use the calculated strain induced in the core and cladding to obtain the change in effective refractive index for the fundamental mode propagating through the optical waveguide as function of  $d$  and  $\Lambda$  and for the three relevant configurations.

As shown in the previous section, at modulation frequencies of the order of 100 MHz the SAW-induced strain extends well into the cladding and should be able to cover the whole cross-sectional area occupied by the optical mode. This strain will lead to a change in the refractive index of the cladding and core via eqs. 2 and 3, the strength of the coupling being set by the strain-optic coefficients. The strain-optic coefficients are not known for  $\text{Si}_3\text{N}_4$ , however, due to our choice of a small core area and high aspect ratio, the influence of the core on the effective refractive index of the optical mode can be neglected. In the model we take the strain-optic coefficients for  $\text{Si}_3\text{N}_4$  equal to zero, to obtain a lower bound of the change in effective refractive index that can be realized. For  $\text{SiO}_2$  we take the strain-optic coefficients to be equal to  $p_{11} = 0.118$  and  $p_{12} = 0.252$  [38–41]. Due to the difference in strain in the  $x$ - and  $y$ -direction, the refractive index experienced by the mode is different for the quasi-TE and quasi-TM polarization [42]. To find the effective refractive index for the fundamental mode for the two polarization directions, we take the calculated strain and add the appropriate change in refractive index to the material refractive index [28] (using eq. 2 for the quasi-TE and eq. 3 for the quasi-TM polarization). Subsequently we use the eigenmode solver [33] to determine the propagation constant,  $\beta$ , and the spatial shape and field distribution for the fundamental quasi-TM mode. We then calculate the effective refractive index of this mode,  $n_{\text{eff}} = c\beta/\omega$ , and determine the difference,  $\Delta n$ , with the effective refractive index for the same mode in absence of a SAW.

Since the waveguide geometry we choose is meant for the visible and near-infrared applications [43], we selected an intermediate wavelength ( $\lambda = 840$  nm as an example). Figure 6 shows the normalized intensity distribution of the fundamental guided mode with vertical polarization (quasi-TM mode), core area of  $4.4 \times 0.03 \mu\text{m}^2$  and using the same coordinate system as for Fig. 4. We observe that the mode is confined around the core and has negligible amplitude already being  $5 \mu\text{m}$  away from the core. The effective refractive index for this mode is found to be  $n_{\text{eff}} = 1.4646$ , which is close to the refractive index of the  $\text{SiO}_2$  cladding. This confirms that most of the optical field is outside the  $\text{Si}_3\text{N}_4$  core and that approximating the influence of the strain in the core as negligible is justified. When the SAW-induced strain is applied, the transverse shape of the intensity distribution as displayed in Fig. 6 is almost unaffected by the slight change in refractive index of the cladding material (in the order of  $10^{-3}$ ), however, the longitudinal propagation constant is changed and, hence, the effective refractive index.

### Effective refractive index dependency on IDT periodicity

In Fig. 7(a-c) we show the calculated relative change in effective refractive index,  $\Delta n/n_{\text{eff}}$ , for the fundamental mode with TM polarization as a function of the IDT period,  $\Lambda$ , for the configurations ETD (a), EBD (b), and EBC (c), respectively. In each case,  $\Delta n/n_{\text{eff}}$  is calculated for three different thicknesses of the PZT layer,  $d = 2.5, 3$  and  $3.0 \mu\text{m}$ , while the voltage signal applied to the IDT period is maintained at a constant amplitude of 10 V with a configuration dependent near-resonant frequency (see Fig. 3). As expected from the calculations of the strain at the center of the waveguide core (see Fig. 4), Fig. 7 shows an initial increase in the relative change in effective refractive index with increasing period of the IDT before reaching a maximum and then starts to decrease when the

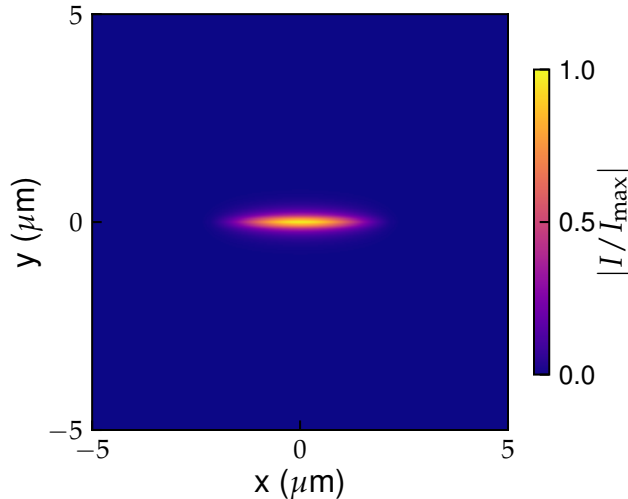


Figure 6: Normalized intensity distribution of the fundamental quasi-TM mode for a wavelength of 840 nm. The  $\text{Si}_3\text{N}_4$  core with dimensions of 30 nm by  $4.4 \mu\text{m}$  is centered at the origin of the coordinate system. The drawing is to scale.

period is further increased. This behaviour is found for all three configurations investigated. However, the maximum  $\Delta n/n_{\text{eff}}$  is largest for the EBC configuration followed by the EBD and the ETD configurations, for which the maximum change in relative refractive index is smaller by a factor of 1.2 and 1.5, respectively. Furthermore, Fig. 7 shows that the maximum change in effective refractive index shifts to a lower value of  $\Lambda$  when going from configuration ETD via EBD to EBC. According to Fig. 3, this leads to a higher modulation frequency, from around 90 MHz to 100 MHz. Finally, we observe that the change in effective refractive index drops more quickly with increasing IDT period beyond the maximum for configuration EBC (Fig. 7(c)) compared to the other two configurations.

### Effective refractive index dependency on PZT thickness

So far, we have only considered the variation with  $\Lambda$  for a few fixed values of the PZT layer thickness. In Fig. 8(a-c) we show the calculated relative change in effective refractive index as a function of the PZT layer thickness,  $d$ , for the configurations ETD (a), EBD (b), and EBC (c), respectively. In each case,  $\Delta n/n_{\text{eff}}$  is calculated for three different IDT periods,  $\Lambda = 25, 30$  and  $35 \mu\text{m}$  and the remaining parameters are as for Fig. 7. With the IDT electrode on top (ETD), *i.e.*, with the electrode at the PZT-air interface, we find that  $\Delta n/n_{\text{eff}}$  is almost constant for  $d < 3 \mu\text{m}$  for each of the three IDT periods investigated. For larger values of  $d$ ,  $\Delta n/n_{\text{eff}}$  starts to differ between the three configurations (Fig. 8(a)), with the lowest IDT period of  $\Lambda = 25 \mu\text{m}$  showing a faster drop in  $\Delta n/n_{\text{eff}}$  than

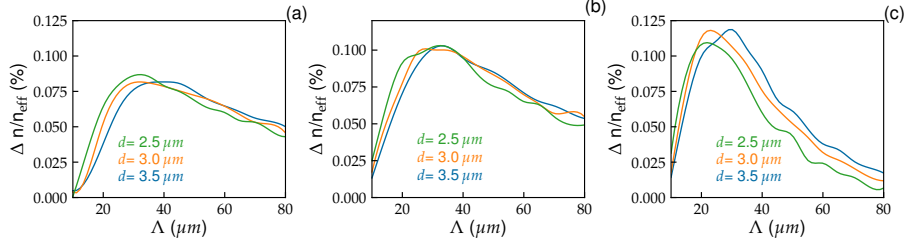


Figure 7: Relative change in the effective refractive index,  $\Delta n/n_{\text{eff}}$ , as a function of IDT period,  $\Lambda$ , for three different PZT-layer thicknesses,  $d = 2.5, 3.0$  and  $3.5 \mu\text{m}$ , and for configuration ETD (a), EBD (b) and EBC (c). The vacuum wavelength is  $\lambda = 840 \text{ nm}$  and the light is polarized in the  $y$ -direction (TM polarization).

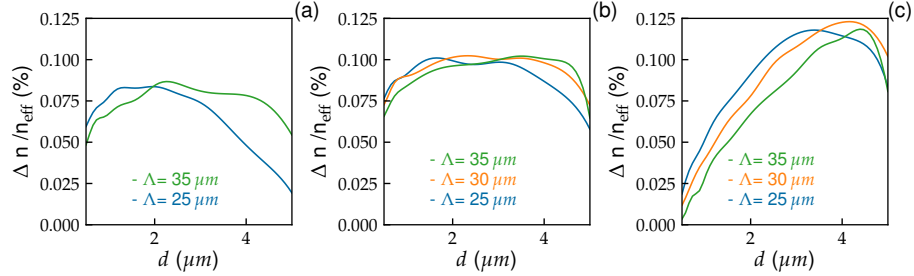


Figure 8: Relative change in the effective refractive index,  $\Delta n/n_{\text{eff}}$ , as a function thickness of the PZT layer,  $d$  for three different IDT periods,  $\Lambda = 25, 30$  and  $35 \mu\text{m}$  and for configuration ETD (a), EBD (b) and EBC (c). The vacuum wavelength is  $\lambda = 840 \text{ nm}$  and the light is polarized in the  $y$ -direction (TM polarization).

for the other two IDT periods investigated. For the case of the IDT electrode placed at the bottom of the PZT layer and no conductive layer placed in the opposite side (EBD), Fig. 8(b) shows that  $\Delta n/n_{\text{eff}}$  is almost independent of  $d$  for the three IDT periods investigated. A decrease in  $\Delta n/n_{\text{eff}}$  is found only for very small ( $< 1 \mu\text{m}$ ) or very large ( $> 4 \mu\text{m}$ ) thickness of the PZT layer. On the other hand, with the IDT electrode at the bottom and a 100-nm conductive gold layer at the opposite site of the PZT layer (EBC), Fig. 8(c) shows a strong variation of  $\Delta n/n_{\text{eff}}$  with  $d$  for all periods investigated. The optimum layer thickness for maximum  $\Delta n/n_{\text{eff}}$  is between 3 and 4  $\mu\text{m}$ , depending on the IDT period.

The largest  $\Delta n/n_{\text{eff}}$  of  $\sim 0.12\%$  is obtained with this configuration for  $\Lambda \approx 30 \mu\text{m}$  and  $d \approx 4 \mu\text{m}$ . This corresponds to an absolute change in index of  $\Delta n = 1.7 \times 10^{-3}$ . Both Figs. 7 and 8 show that the induced change in effective refractive index depends on (i) the location of the IDT electrode, (ii) its period, (iii) the thickness of the PZT layer and (iv) whether there is a thin conductive layer opposite the IDT electrode or not. To find the maximum value for  $\Delta n/n_{\text{eff}}$  requires a two-dimensional scan over the IDT period and PZT layer thickness for each of the configurations. Although we have not fully scanned

the complete parameter space, Figs. 7 and 8 indicate that the scans presented in these figures should be close to or even contain the optimum combination of  $\Lambda$  and  $d$  to achieve a maximum change in the effective refractive index for each of the configurations investigated.

In summary, having an IDT electrode on top of the PZT layer with a 100-nm thick Pt layer at the SiO<sub>2</sub>-PZT interface (ETC) results in a extremely weak SAW in the cladding region. This configuration was therefore not studied further. Having instead a very thin dielectric seed layer at the SiO<sub>2</sub>-PZT interface (ETD) results in a SAW that penetrates well into the cladding region, however the magnitude of the induced strain and hence the of the maximum relative change in the effective refractive index of  $\sim 0.08\%$  is smallest of the remaining configurations. Optimum values for the IDT period and PZT layer thickness are  $25\ \mu\text{m} < \Lambda < 40\ \mu\text{m}$  and  $1\ \mu\text{m} < d < 2\ \mu\text{m}$ , respectively, depending on the configuration. Moving the IDT electrode to the SiO<sub>2</sub>-PZT interface and having no opposite conductive layer (EBD) generates a maximum relative change in effective refractive index of  $\sim 0.10\%$  for a wide range of IDT periods ( $25\ \mu\text{m} < \Lambda < 40\ \mu\text{m}$ ) and thicknesses of the PZT layer ( $1\ \mu\text{m} < d < 4\ \mu\text{m}$ ). Finally, terminating the SiO<sub>2</sub>-air interface with a 100-nm gold layer (EBC) results in a configuration that generates the largest relative change in effective refractive index of  $\sim 0.12\%$ , although with the smallest parameter range of  $20\ \mu\text{m} < \Lambda < 30\ \mu\text{m}$  and  $3.5\ \mu\text{m} < d < 4\ \mu\text{m}$ . With the additional gold layer at the SiO<sub>2</sub>-air interface, the electric field provided via the IDT electrode is confined to the PZT layer and this produces a SAW wave that generates the largest strain at the location of the waveguide core, though with a stronger dependence on the IDT period and PZT layer thickness. Although this configuration and the required thickness of the PZT layer results in a slightly lower resonant acoustic frequency (*c.f.* Fig. 3), and hence the modulation frequency, the larger induced change in effective refractive index makes this the favorable configuration of the four investigated.

### Optimized design and geometry

Now that we have calculated the maximum value for  $\Delta n/n_{\text{eff}}$  provided by the optimal configuration, which is 0.12%, we use eq. 6 to calculate the required length of the arms of a balanced Mach-Zehnder interferometer to obtain complete light modulation at the acoustic resonance frequency.

For a vacuum wavelength of  $\lambda = 840\ \text{nm}$ , we find  $L = 120\ \mu\text{m}$  using  $n_{\text{eff}} = 1.464$  for the quasi-TM polarized light. The voltage applied to the IDT has an amplitude of 10 V. Due to the linearity of the strain with applied voltage expected in this regime of small strain and index modulation, obtaining full light modulation at a shorter wavelength, say half the used wavelength (420 nm) would required driving the IDTs only at half the voltage ( $\sim 5\ \text{V}$ ). In contrast, modulating light with a longer wavelength, say at telecom wavelengths (1550 nm), would almost double the required driving voltage ( $\sim 18.5$ ). Nevertheless, both values are well within the expected operating range that may extend to voltage amplitudes of 50 V or more before breakdown occurs [19, 30, 37]. This means that depending on the selected voltage or wavelength even a smaller arm length than 120  $\mu\text{m}$  might be sufficient to obtain full light modulation.

## 5 Summary and Conclusions

In this work we investigated the use of a Rayleigh-type surface acoustic waves (SAWs) to modulate the effective refractive index of an optical mode guided by a buried  $\text{Si}_3\text{N}_4$  waveguide core in a  $\text{SiO}_2$  cladding. We considered that the acoustic waves are excited in a PZT piezo-electric film layer deposited on top of the waveguide cladding via interdigitized electrodes, at a frequency in the order of 100 MHz.

Considering a balanced Mach-Zehnder interferometer, the modulation of the effective refractive index can be used to obtain full, *i.e.*, 100%-modulation of the light power and amplitude, at the acoustic frequency. The optical waveguide considered here consists of a  $\text{Si}_3\text{N}_4$  core, with dimensions of  $4.4 \mu\text{m}$  by  $30 \text{ nm}$ , buried in a  $\text{SiO}_2$  cladding  $8 \mu\text{m}$  below the surface, which is typical for this low-loss photonic platform. The SAWs generated by the thin PZT layer is guided in the interface between the PZT and the cladding, while its evanescent strain field extends towards depths that include the waveguide core. The strain induced by the SAW results in a change of the effective refractive index of the waveguide via the strain-optic effect.

We find that of four investigated IDT-PZT arrangements, the combination of IDT electrode at the interface  $\text{SiO}_2$ -PZT with a counterelectrode at the PZT-air interface (configuration EBC) is the most efficient in generating strain in the cross sectional area of the optical mode. This results in a maximum relative change in effective refractive index for the fundamental waveguide mode of  $\Delta n/n_{\text{eff}} = 0.12\%$  for a wavelength in the middle of the working range of this waveguide, here taken as  $\lambda = 840 \text{ nm}$ , with quasi-TM polarization. The maximum modulation is obtained near-resonance at a driving voltage of  $10 \text{ V}$  for an IDT electrode periodicity  $\Lambda = 30 \mu\text{m}$  with a PZT thickness  $d = 4 \mu\text{m}$ .

For the maximum relative change in refractive index, the arm length required in a balanced Mach-Zehnder interferometer is  $120 \mu\text{m}$ , with 100% light modulation driven with  $10 \text{ V}$  at a frequency of  $90 \text{ MHz}$ . We note that this frequency is larger by at about five orders of magnitude compared to thermo-optic intensity modulators and about two orders of magnitude compared to a stress-optic intensity modulator where stress is induced via a single electrode [18].

We note that also the required interaction length (for a MZI) is shorter, by a factor about five to ten, than what is typically used in thermally operated MZI ( $500 \mu\text{m}$ ) and by a factor of 80 compared to proximity strain-optic modulation [18]. As a parallel route for optimization, IDT electrodes might be configured to generate a focused SAW [44] to increase the strain in the region of the optical mode. An additional variation would be meandering the optical waveguide though the SAW field for shortening of the required overlap length with the transverse SAW field dimension. Also, the cladding height above the core might be reduced by one third without affecting notably the optical propagation loss, because the optical mode with our example wavelength, and also for even shorter wavelengths as in [18] does not extend too far outside the core (*c.f.* Fig. 6). Another advantage of using a SAW to drive a Mach-Zehnder interferometer is that it can coherently drive multiple interferometers located suitably next to each other for providing a stable phasing relative to each other. This is of interest, *e.g.*, for low-loss phase modulators that form optical isolators based on acoustic waves [45, 46].

## References

1. Bauters, J. F., Heck, M. J. R., John, D., Dai, D., Tien, M.-C., Barton, J. S., Leinse, A., Heideman, R. G., Blumenthal, D. J. & Bowers, J. E. Ultra-low-loss high-aspect-ratio Si<sub>3</sub>N<sub>4</sub> waveguides. *Opt. Express* **19**, 3163–3174 (2011).
2. Wörhoff, K., Heideman, R., Leinse, A. & Hoekman, M. TriPleX: A versatile dielectric photonic platform. *Adv. Opt. Techn.* **4**, 189–207 (2015).
3. Heck, M. J. R., Bauters, J. F., Davenport, M. L., Spencer, D. T. & Bowers, J. E. Ultra-low loss waveguide platform and its integration with silicon photonics. *Laser Photonics Rev.* **8**, 667–686 (2014).
4. Epping, J. P. *et al.* On-chip visible-to-infrared supercontinuum generation with more than 495 THz spectral bandwidth. *Opt. Express* **23**, 19596–19604 (2015).
5. Nguyen, V. D., Weiss, N., Beeker, W., Hoekman, M., Leinse, A., Heideman, R. G., van Leeuwen, T. G. & Kalkman, J. Integrated-optics-based swept-source optical coherence tomography. *Opt. Lett.* **37**, 4820–4822 (2012).
6. Zinoviev, K., Carrascosa, L. G., Sánchez del Río, J., Sepúlveda, B., Domínguez, C. & Lechuga, L. M. Silicon Photonic Biosensors for Lab-on-a-Chip Applications. *Advances in Optical Technologies* **2008**, 383927 (2008).
7. Roeloffzen, C. G. H., Zhuang, L., Taddei, C., Leinse, A., Heideman, R. G., van Dijk, P. W. L., Oldenbeuving, R. M., Marpaung, D. A. I., Burla, M. & Boller, K.-J. Silicon nitride microwave photonic circuits. *Opt. Express* **21**, 22937–22961 (2013).
8. Marpaung, D., Roeloffzen, C., Heideman, R., Leinse, A., Sales, S. & Capmany, J. Integrated microwave photonics. *Laser Photon. Rev.* **7**, 506–538 (2013).
9. Oldenbeuving, R. M., Klein, E. J., Offerhaus, H. L., Lee, C. J., Song, H. & Boller, K.-J. 25 kHz narrow spectral bandwidth of a wavelength tunable diode laser with a short waveguide-based external cavity. *Laser Physics Letters* **10**, 015804 (2013).
10. Halir, R., Okawachi, Y., Levy, J. S., Foster, M. A., Lipson, M. & Gaeta, A. L. Ultrabroadband supercontinuum generation in a CMOS-compatible platform. *Opt. Lett.* **37**, 1685–1687 (2012).
11. Zhuang, L. *et al.* On-chip microwave photonic beamformer circuits operating with phase modulation and direct detection. *Opt. Express* **22**, 17079–17091 (2014).
12. Xiong, C. *et al.* Compact and reconfigurable silicon nitride time-bin entanglement circuit. *Optica* **2**, 724–727 (2015).
13. Zhuang, L., Roeloffzen, C. G. H., Hoekman, M., Boller, K.-J. & Lowery, A. J. Programmable photonic signal processor chip for radiofrequency applications. *Optica* **2**, 854–859 (2015).
14. Ovvyan, A., Gruhler, N., Ferrari, S. & Pernice, W. Cascaded Mach-Zehnder interferometer tunable filters. *J. Opt.* **18**, 064011 (2016).

15. Brewster, D. On the effects of simple pressure in producing that species of crystallization which forms two oppositely polarised images, and exhibits the complementary colours by polarised light. *Phil. Trans. R. Soc. Lond.* **105**, 60–64 (1815).
16. Yariv, A. & Yeh, P. *Photonics: Optical Electronics in Modern Communications* (Oxford University Press, Inc., New York, NY, USA, 2007).
17. Schriever, C., Bohley, C., Schilling, J. & Wehrspohn, R. B. Strained Silicon Photonics. *Materials* **5**, 889–908 (2012).
18. Hosseini, N., Dekker, R., Hoekman, M., Dekkers, M., Bos, J., Leinse, A. & Heideman, R. Stress-optic modulator in TriPleX platform using a piezoelectric lead zirconate titanate (PZT) thin film. *Opt. Express* **23**, 14018–14026 (2015).
19. De Lima Jr., M. M., Beck, M., Hey, R. & Santos, P. V. Compact Mach-Zehnder acousto-optic modulator. *Appl. Phys. Lett.* **89**, 121104 (2006).
20. Tadesse, S. A. & Li, M. Sub-optical wavelength acoustic wave modulation of integrated photonic resonators at microwave frequencies. *Nat. Commun.* **5**, 5402 (2014).
21. Tadesse, S. A., Li, H., Liu, Q. & Li, M. Acousto-optic modulation of a photonic crystal nanocavity with Lamb waves in microwave K band. *Appl. Phys. Lett.* **107**, 201113 (2015).
22. Rayleigh, L. On waves propagated along the plane surface of an elastic solid, 4–11 (1885).
23. Lima, M. M. d. & Santos, P. V. Modulation of photonic structures by surface acoustic waves. *Reports on Progress in Physics* **68**, 1639–1701 (2005).
24. Kay, H. Electrostriction. *Rep. Prog. Phys.* **18**, 230 (1955).
25. Sundar, V. & Newnham, R. E. Electrostriction and polarization. *Ferroelectrics* **135**, 431–446 (1992).
26. Boyd, R. W. *Nonlinear Optics* (Academic Press, 2013).
27. Borrelli, N. F. & Miller, R. A. Determination of the individual strain-optic coefficients of glass by an ultrasonic technique. *Appl. Opt.* **7**, 745–750 (1968).
28. Korpel, A. *Acousto-Optics, Second Edition* (CRC Press, 1996).
29. Telford, W., Geldart, L. & Sheriff, R. *Applied Geophysics* (Cambridge University Press, 1990).
30. Hashimoto, K. *Surface acoustic devices in telecommunications: modelling and simulation* (Springer-Verlag, Berlin; Germany, 2000).
31. Saito, Y., Takao, H., Tani, T., Nonoyama, T., Takatori, K., Homma, T., Nagaya, T. & Nakamura, M. Lead-free piezoceramics. *Nature* **432**, 84–87 (2004).
32. Fukushima, J., Kodaira, K. & Matsushita, T. Preparation of ferroelectric PZT films by thermal decomposition of organometallic compounds. *Journal of Materials Science* **19**, 595–598 (1984).
33. *COMSOL Multiphysics*® version 5.0. www.comsol.com, 1986.

34. Luke, K., Okawachi, Y., Lamont, M. R. E., Gaeta, A. L. & Lipson, M. Broadband mid-infrared frequency comb generation in a  $\text{Si}_3\text{N}_4$  microresonator. *Opt. Lett.* **40**, 4823–4826 (2015).
35. Lazan, B. J. *Damping of materials and members in structural mechanics* 340 pp. (Pergamon Press, 1968).
36. Zhang, L., Barrett, R., Cloetens, P., Detlefs, C. & Sanchez del Rioa, M. Anisotropic elasticity of silicon and its application to the modelling of X-ray optics. *J. Synchrotron Radiat.* **21**, 507–517 (2014).
37. <http://www.efunda.com/> 2017.
38. Bertholds, A. & Dandliker, R. Determination of the individual strain-optic coefficients in single-mode optical fibres. *J. Lightwave Technol.* **6**, 17–20 (1988).
39. Heiman, D., Hamilton, D. & Hellwarth, R. Brillouin scattering measurements on optical glasses. *Phys. Rev. B* **19**, 6583–6592 (1979).
40. Galbraith, J. *Photoelastic properties of oxide and non-oxide glasses* PhD thesis (Dalhousic University, Nova Scotia, 2014).
41. Schroeder, J. Brillouin scattering and Pockels coefficients in silicate glasses. *J. Non-Cryst. Solids* **40**, 549–566 (1980).
42. Fallahkhair, A. B., Li, K. S. & Murphy, T. E. Vector Finite Difference Modesolver for Anisotropic Dielectric Waveguides. *J. Lightwave Technol.* **26**, 1423–1431 (2008).
43. Haglund, E. P., Kumari, S., Gustavsson, J. S., Haglund, E., Roelkens, G., Baets, R. G. & Larsson, A. *Hybrid vertical-cavity laser integration on silicon* in. Vertical-Cavity Surface-Emitting Lasers XXI (International Society for Optics and Photonics, 2017), 101220H.
44. Collins, D. J., Neild, A. & Ai, Y. Highly focused high-frequency travelling surface acoustic waves (SAW) for rapid particle sorting. *Lab. Chip* **16**, 471 (2016).
45. Hendrickson, S. M., Foster, A. C., Camacho, R. M. & Clader, B. D. Integrated nonlinear photonics: emerging applications and ongoing challenges. *J. Opt. Soc. Am. B* **31**, 3193–3203 (2014).
46. Shi, Y., Cerjan, A. & Fan, S. Acousto-optic finite-difference frequency-domain algorithm for first-principles simulations of on-chip acousto-optic devices. *APL Photonics* **2**, 020801 (2017).